PCCP

ROYAL SOCIETY OF CHEMISTRY

PAPER

View Article Online
View Journal | View Issue

Cite this: *Phys. Chem. Chem. Phys.*, 2024, **26**, 14448

Mechanistic study of the atomic layer deposition of cobalt: a combined mass spectrometric and computational approach†

Sofia Donnecke,*[a] Mathias Paul,[a] Peter J. H. Williams,[a] Serena Chan,[a] Veronica Tse,[a] Jigyasa Sachdeva,[a] Allen G. Oliver,[b] J. Scott McIndoe*[a] and Irina Paci*[a]

Cobaltcarbonyl-*tert*-butylacetylene (CCTBA) is a conventional precursor for the selective atomic layer deposition of Co onto silicon surfaces. However, a limited understanding of the deposition mechanism of such cobalt precursors curbs rational improvements on their design for increased efficiency and tuneable selectivity. The impact of using a less reactive internal alkyne instead of a terminal alkyne was investigated using experimental and computational methods. Using electrospray-ionization mass spectrometry, the formation of CCTBA analogs and their gas phase decomposition pathways were studied. Decomposition experiments show very similar decomposition pathways between the two complexes. The internal alkyne dissociates from the Co complex at slightly lower energies than the terminal alkyne, suggesting that an internal alkynyl ligand may be more suited to low temperature ALD. In addition, transition state calculations using the nudged elastic band method confirm an increased reaction barrier between the internal alkyne and the Si–H surface bonds on Si(111). These results suggests that using a less reactive internal alkyne will result in fewer embedded carbon impurities during deposition onto Si wafers. DFT calculations using the PBE functional and periodic boundary conditions also predict increased surface binding with the metal centers of the internal alkynyl complex.

Received 8th January 2024,
Accepted 15th April 2024

DOI: 10.1039/d4cp00093e

rsc.li/pccp

Atomic layer deposition (ALD) is an emerging technique for depositing thin films with high conformity in a self-limiting manner. However, the development of precursors with better performance or specific function is limited by a lack of fundamental knowledge over mechanistic pathways taking place on the surface during ALD. Cobalt is specifically used as a seed layer for copper interconnects to prevent defects and atom migration across the interface between the conductive and dielectric layers of devices.[1,2] However, there is a limited number of established Co precursors for ALD. The organometallic complex $Co_2(CO)_6(\mu^2\text{-HCCCMe}_3)$ (known as CCTBA, cobaltcarbonyl-*tert*-butylacetylene) is a common precursor for the chemical vapour deposition (CVD) and ALD of cobalt.[1,3–10] Its high vapour pressure and relatively small molecular size enhances the performance of CCTBA as a volatile source of Co, making it desirable compared to many other Co precursors.[5] Furthermore, the synthesis of cobalt-alkyne complexes is straightforward and well-established across a wide range of alkynes.[11] The ease of cleaving ligands as neutral molecules minimizes surface impurities and improves the atom economy during the ALD process. However, Co precursors, including CCTBA, participate undesired side-reactions during deposition which embed impurities in the surface. While CCTBA can be used to deposit metallic cobalt under a fairly wide range of ALD temperatures (70–250 °C), it has been shown that deposition at lower temperatures (70–110 °C) results in large amounts of carbon contamination.[7] Hydrosilation is thought to occur between the alkyne and Si–H terminated surfaces, leaving behind carbon to disrupt the desired material uniformity and properties such as conductivity.[10] Modifying the properties of the alkyne can help reduce undesired impurities and direct the surface reactivity towards the metal center.[10,12]

Altering the ligands of CCTBA can also tune the precursor for deposition onto specific surfaces. However, these modifications require insight on the mechanisms by which precursors such as CCTBA undergo during ALD.[13] Studying heterogeneous reactions on surfaces is notoriously difficult using experimental methods. Mass spectrometric studies have been used for *in situ* monitoring of the gaseous biproducts from ALD of Al_2O_3[14,15]

[a] *Department of Chemistry, University of Victoria, Victoria, V8P 5C2, Canada. E-mail: ipaci@uvic.ca; Tel: +250-472-4946*

[b] *Department of Chemistry and Biochemistry, University of Notre Dame, Notre Dame, IN 46556, USA*

† Electronic supplementary information (ESI) available. CCDC 2314737 and 2314738. For ESI and crystallographic data in CIF or other electronic format see DOI: https://doi.org/10.1039/d4cp00093e

and ZrO_2.[16] Researchers often turn to computational chemistry methods to develop an understanding of deposition processes at the atomic level. Density functional theory (DFT) can be paired with transition state methods such as nudged elastic band (NEB) to develop a mechanistic understanding of precursor decomposition and deposition.[17] Methods such as *ab initio* molecular dynamics are also used for simulating interactions between precursors and the surface.[18] However, there is a general lack in combined experimental and theoretical data probing Co-ALD mechanisms.[19] For the cobalt carbonyl complex to interact strongly with a surface, it must first lose ligands and the mechanism by which this occurs is currently obscure. Understanding which ligands are lost first, whether the alkyne leaves intact or in parts, and how changing the ligand might affect these gas-phase processes will provide useful insights about the chemical processes occurring during ALD. Modelling the surface interactions will also improve our understanding of deposition and how to limit impurities.

We set out to identify the effect of replacing the terminal alkyne with an internal alkyne on the gas phase decomposition and surface deposition of the precursor. The postulated hydrosilation mechanism taking place on a treated Si–H surface is expected to be more hindered by an internal alkyne. While cobaltcarbonyl-*tert*-butylmethylacetylene (CCTMA) has a slightly higher melting point than CCTBA, making it more difficult to vaporize, it has already been shown to produce lower resistivity films on silica than CCTBA, which suggests a lower carbon content.[4] By synthesizing charged analogs of these alkynyl cobalt carbonyl complexes we can probe their gas phase reactivity through collision induced dissociation (CID) and determine whether CCTMA demonstrates similar gas phase decomposition pathways to that of CCTBA. Insight upon the gas phase decomposition of these alkynyl cobalt carbonyl complexes can determine whether CCTMA demonstrates similar behaviour to CCTBA. Modelling the surface interactions on a Si(111) surface demonstrates the effect of an internal *versus* terminal alkyne on cobalt deposition as well as the reaction pathway for carbon contamination.

1 Methods

1.1 Synthesis of CCTBA analogs

The conventional synthesis of CCTBA for ALD involves substitution of two carbonyl ligands for TBA (*tert*-butylacetylene) (Fig. 1 where R = H).[9] This reaction is fast (minutes) at room temperature and possible across a variety of alkynes, including internal alkynes. The traditional complex containing a terminal alkyne (R = H) was compared against an internal alkyne (R = Me) to identify differences in reactivity.

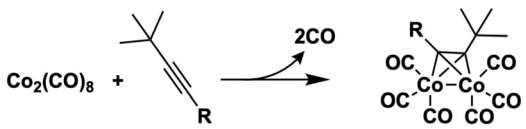

Fig. 1 The formation of CCTBA. This reaction can be performed neat or in a non-polar solvent at room temperature.

The prospect of a model system to enable direct probing of the decomposition of CCTBA was appealing, and accordingly we designed and synthesized a charge-tagged acetylene ligand that would react with $Co_2(CO)_8$ analogously to CCTBA. A charged alkyne enables direct analysis of the ligand using electrospray ionization mass spectrometry (ESI-MS)[20] to observe its reactivity with $Co_2(CO)_8$ in real-time.[21] In addition, the gas-phase decomposition of the product complex can be monitored using collision-induced dissociation (CID) in the mass spectrometer.

Two charged tags were prepared, one a terminal alkyne $[HCC(CH_2)_4PPh_3]PF_6$ ([**1**]PF_6) and the other an internal alkyne $[CH_3CC(CH_2)_2PPh_3]PF_6$ ([**2**]PF_6) as described in the ESI.† We chose hexafluorophosphate as a counterion to eliminate any chance of the halide ion acting as a ligand itself, and to improve the solubility of **1** and **2** in the low-polarity solvents preferred for ESI-MS.

1.2 Characterization of CCTBA analogs

Once compounds [**1**]PF_6 and [**2**]PF_6 were synthesized, **2** was recrystallized with both I^- and PF_6^- counterions. The solid state molecular structures were obtained using X-ray crystallography.† We were able to successfully characterize these internal ([**1**]PF_6) and terminal ([**2**]PF_6) alkynyl complexes by anaerobic ESI-MS[22] (Fig. 2). These complexes were prepared to be used as charged analogs of CCTMA (**3**) and CCTBA (**4**) for further gas phase analysis.

All mass spectrometry samples were prepared in distilled DCM at room temperature under nitrogen. Due to the low boiling point of the solvent, the desolvation gas flow rate was kept between 80 and 100 L h^{-1} and the cone gas flow rate was set to 100 L h^{-1}. The source temperature was set to 40 °C and the desolvation temperature was held between 100 and 120 °C. Argon was used as a collision gas. For further details on the experimental setup see the ESI.†

1.3 Computational methods

Density functional theory (DFT) was employed to compute the geometries of gas phase decomposition species using a PBE0/def2-TZVP approach with dispersive interaction treated using

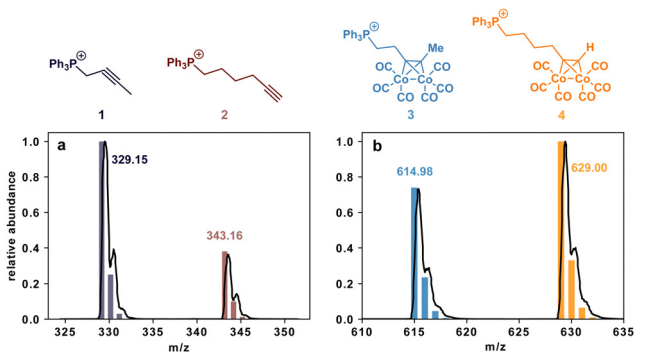

Fig. 2 Mass spectra of species **1**, **2**, **3** and **4** plotted with their expected isotope patterns. Panel a plots the *m/z* of the internal and terminal alkyne charged tags and b plots the charged analogs of CCTBA and CCTMA.

the Becke–Johnson D3 model[23] in the NWChem/v6.8.1 program.[24] For calculations involving surface reactions, a PBE-vdW-TS/DZP approach was used in the SIESTA 4.0.1 program.[25] Periodic Si(111) slabs consisting of four atomic layers and repeating every six atoms in the x and y direction were surface-capped with hydrogen. Troullier–Martins effective core potentials from the SIESTA database[26] were used alongside a DZP basis for atomic and cell optimizations. A spacing of 50 was included between slabs in the direction perpendicular to the surface. All calculations were done at the Γ point. The orbital energy shift was set to a cutoff energy of 0.001 Ry. Nosé–Hoover molecular dynamics calculations were performed in SIESTA (130 K) to sample the binding configurations of key intermediates on the surface.[27] Surface-bound transition states were identified using the nudged elastic band (NEB) approach. NEB calculations were performed using the Atomic Simulation Environment (ASE)[28] in conjunction SIESTA.

2 Results and discussion

2.1 Experimental monitoring of CCTBA formation

Having the readily available charged alkynes provided the opportunity to directly probe the formation of CCTBA with ESI-MS. The reaction of [**1**]PF_6 and [**2**]PF_6 at concentrations of 10 μM with excess $Co_2(CO)_8$ in dichloromethane was monitored in real time using PSI-ESI-MS.[29,30] The reaction proceeded cleanly to $Co_2(CO)_6(\mu^2$-alkyne) as seen in the standard synthesis of CCTBA (Fig. 1). No intermediate $Co_2(CO)_7$ (μ^1-alkyne) ions were observed in either case, even at trace levels.

Two conclusions can be drawn from monitoring the charged alkynes forming alkynyl complexes. Firstly, the reaction of **1** with $Co_2(CO)_8$ was approximately three times slower than the reaction between **2** and $Co_2(CO)_8$. This is expected with increased steric hindrance introduced by the methyl group and by the phenyl groups in closer proximity. However, even at millimolar concentrations of $Co_2(CO)_8$, the reaction proceeded to completion within 20 minutes. Secondly, the rate of the reaction depends on the concentration of $Co_2(CO)_8$. When doubling the $Co_2(CO)_8$ from 1 mM to 2 mM while keeping **1** and **2** at 10 μM, the rate of reaction doubles, indicating the reaction is first order in $Co_2(CO)_8$. This observation was corroborated by performing variable time normalization analysis (VTNA)[31] to overlay the chromatograms (Fig. 3). Normalizing the time axis by the constant concentration of $Co_2(CO)_8$ raised to the first power results in good overlay for the PSI traces in the formation of **3** (Fig. 3c) and **4** (Fig. 3d). This confirms that the reaction is first order in $Co_2(CO)_8$. An order of 0.7 in alkyne was established and the overall rate law of the reaction was determined.

$$\text{Rate} = k[Co_2(CO)_8]^1[\text{alkyne}]^{0.7}$$

The approximate rate constants for the reactions were determined to be $k = 3$ in the formation of the internal alkynyl complex and and $k = 13$ for the terminal alkynyl complex. Using the determined rate laws, modelled reactant curves were overlaid on the reactant traces in Fig. 3. The internal alkyne binds to cobalt carbonyl considerably slower than the terminal alkyne at

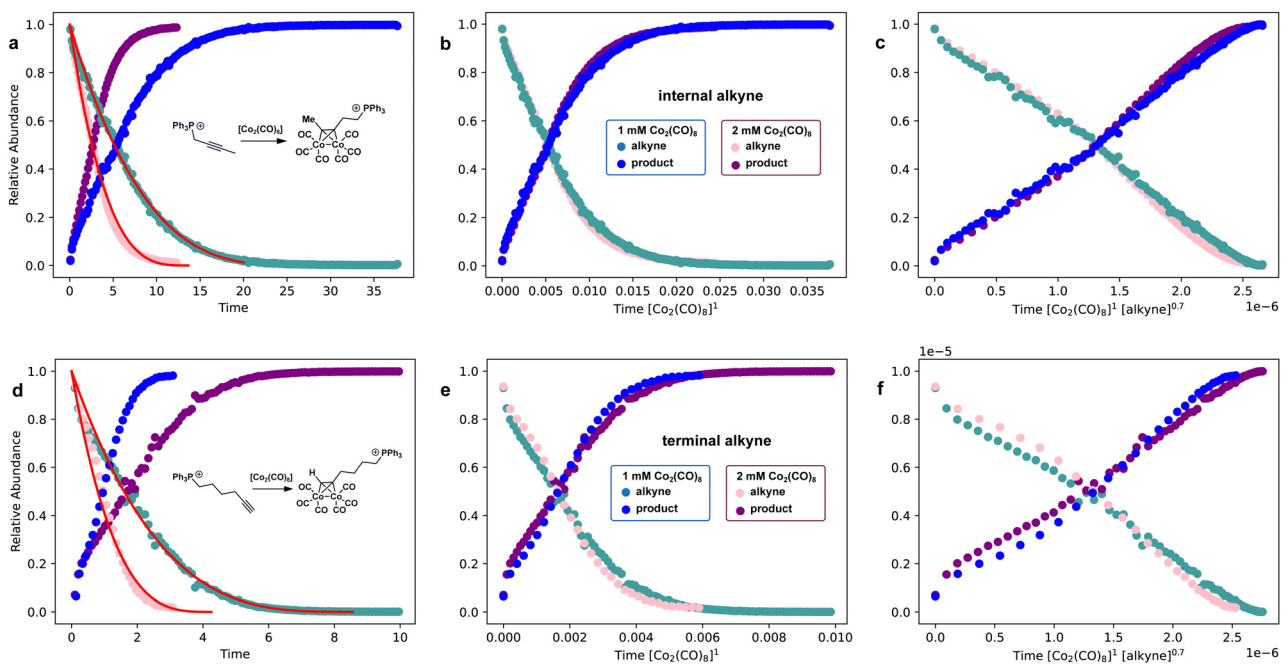

Fig. 3 PSI-ESI-MS chromatograms show the rate dependence on the concentration of cobalt carbonyl. Formation of **3** (a) and **4** (d) was monitored with starting concentrations of 1 mM (blue) and 2 mM (purple) $Co_2(CO)_8$. A concentration of 10 μM was used for the terminal and internal alkynyl ions. Note that the first thirty seconds of reactivity are missing due to the lag between addition of the $Co_2(CO)_8$ and arrival of the reacting solution in the mass spectrometer. Panels (b) and (e) show the time normalized traces for the reaction with respect to cobalt carbonyl to the first order. An order of 0.7 in alkyne was established (c) and (f) and rate constants were determined to be 3 and 13 for the internal and terminal alkynes respectively. Modelled reactant curves were also overlaid on the reactant traces in red (panels a and a).

equal concentrations. We attribute this to the increased bulk on the triple bond.

2.2 Computational modelling of CCTBA formation

The formation of CCTBA was computationally modelled without the charge tag to obtain the energy of isomers, potential intermediates, and the overall reaction. Geometry optimizations were used to analyze the effect of an internal alkyne on the overall structure and bonding character at the metal center. Two geometries were optimized for $Co_2(CO)_8$ with differing symmetry. The C_{2v} isomer has been reported in crystal structures,[32] and is 7 kJ mol^{-1} lower in energy than the D_{3d} isomer. This relative stability has been confirmed by solution phase studies with IR spectroscopy.[33,34] For the alkyne to associate to the metal complex, CO must first dissociate. We expect CO dissociation to be the rate determining step of the reaction, thus predicting the overall formation of CCTBA. The electronic energy cost of losing a carbonyl to form a $Co_2(CO)_7$ intermediate was calculated to be +110 kJ mol^{-1} and the overall transformation to CCTBA was +39 kJ mol^{-1} for both the internal and terminal alkyne (see ESI†). No heptacarbonyl species were observed during PSI-ESI-MS experiments which suggests that either both carbonyls are removed before the alkynyl complex fully forms or that the steps following alkyne binding (CO loss and rearrangement) are concerted or very fast.

The geometry optimizations for both the internal and terminal alkynyl complexes revealed consistent changes in hybridization in the coordinating carbons. C–C and Co–Co bond lengths remain nearly identical between the internal and terminal alkyne (see ESI†). Both alkynes change from a linear configuration (R–C–C = 180°) to a bent configuration with increased p character (R–C–C = 143°) when coordinating across the Co–Co bond, which agrees with the known trend for general cobalt carbonyl alkynyl complexes.[11] Furthermore, upon coordination the C1–C2 triple bond lengthens to resemble a typical alkene double bond (C–C = 1.34 Å). These findings suggest that the metal centers in CCTBA are closer to an oxidation state of Co(+1) than Co(0) as usually presumed for late transition metal complexes.[10] Oftentimes, alkynes are considered dative ligands which normally do not affect the oxidation state of a metal, binding side-on and serving as a 2e$^-$ σ-donor. However, the metal center can donate electrons into the π* orbital of carbon to rehybridize the triple bond,[35,36] forming a metallacyclopropene complex.[37,38] Regardless of the metal oxidation state, all ligands on CCTBA can dissociate as neutral ligands, making thermal ALD an effective ligand stripping/reduction technique.

2.3 Gas phase decomposition of ALD precursors

The gas phase decomposition of the precursors were probed by mass spectrometry and modelled computationally. There are no conventional experimental methods to capture information about the gas phase processes that occur in an ALD chamber. To our knowledge, the decomposition pathway of CCTBA has not been studied despite it being an important process to initiate precursor deposition. Mass spectrometric techniques can provide a rare glimpse into what gas phase species are produced by a high energy environment to interact with the surface. CID increases the internal energy of the ionic complexes through multiple energetic interactions with a collision gas (argon in this case), resulting in a series of unimolecular decomposition reactions. CID also offers specific control over the collision energy which allows one to track the decomposition products as the internal energy gradually increases.

The synthesis of charged CCTBA and CCTMA analogs using **2** and **3** respectively has allowed the inspection of their gas-phase decomposition pathways using CID experiments summarized in Fig. 4. This process resulted in two main fragmentation pathways: loss of the alkyne, and carbonyl dissociation. While the two mass spectra in Fig. 4 show some differences in the relative abundances of decomposition products, the speciation of the **3** (*m/z* 629, Fig. 4a) and **4** (*m/z* 615, Fig. 4c) remains consistent between each precursor, with corresponding peaks separated by a mass-to-charge ratio of 14 Da (the mass difference between the internal and terminal charged tags). For both **3** and **4**, the intermediates from the sequential loss of all six carbonyls are observed and the loss of four carbonyls results in an exceptionally stable $Co_2(CO)_2$–alkynyl intermediate (*m/z* 503 and 517 produced from **4** and **3**). For the internal alkynyl complex **4**, the loss of one CO also results in a prominent decomposition product (*m/z* 587) while for **3**, loss of two carbonyls was more a prominent step (*m/z* 573) and occurs slightly earlier than the loss of the alkynyl. Both species result in very low abundance of daughter ions where the Co–Co bond was broken (*m/z* 444, 458). Two peaks at *m/z* 367 and 381 arise from loss of C_6H_6 and H_2 from 447 and 461 in the fragmentation of CCTMA and CCTBA respectively. This sort of rearrangement and C–H activation is quite plausible at high energy, and a lower relative abundance of this daughter ion is observed in the CCTMA spectrum. We observed no evidence of other breakdown products, such as decomposition of the charged tag itself, or loss of neutrals that would suggest C–H activation processes at work (such as H_2 loss).

The decomposition products are plotted with respect to the collision energy in Fig. 4c and d to rank relative bond strengths. Loss of the first carbonyl occurs at very low collision voltage (5 V) for both complexes. Loss of the alkyne ligand occurs after 10 V and competes closely with the loss of four carbonyls in both complexes. Intermediates resulting from cleavage of the Co–Co bond were not abundant, which is reflected in the calculated metal–metal bond strength *versus* the weaker metal–carbonyl bonds. According to the computational results, the loss of CO requires on average +50 kJ mol^{-1} less than cleavage of the Co–Co bond at any given decomposition step (Fig. 5). The ability for the alkyne to be removed intact even after loss of several CO ligands is interesting because it suggests that C–H activation of the alkyne is not necessary in the decomposition pathway, and this is doubtless a contributing factor towards the success of CCTBA as a cobalt ALD precursor. C–H activation can result in tenaciously bound, carbon-containing fragments that are difficult to release from the metal and contaminate the metal layer with unwanted carbon.[8]

These experimental findings were supported by computational results. The decomposition pathways of the neutral internal and terminal alkynyl complexes were investigated to

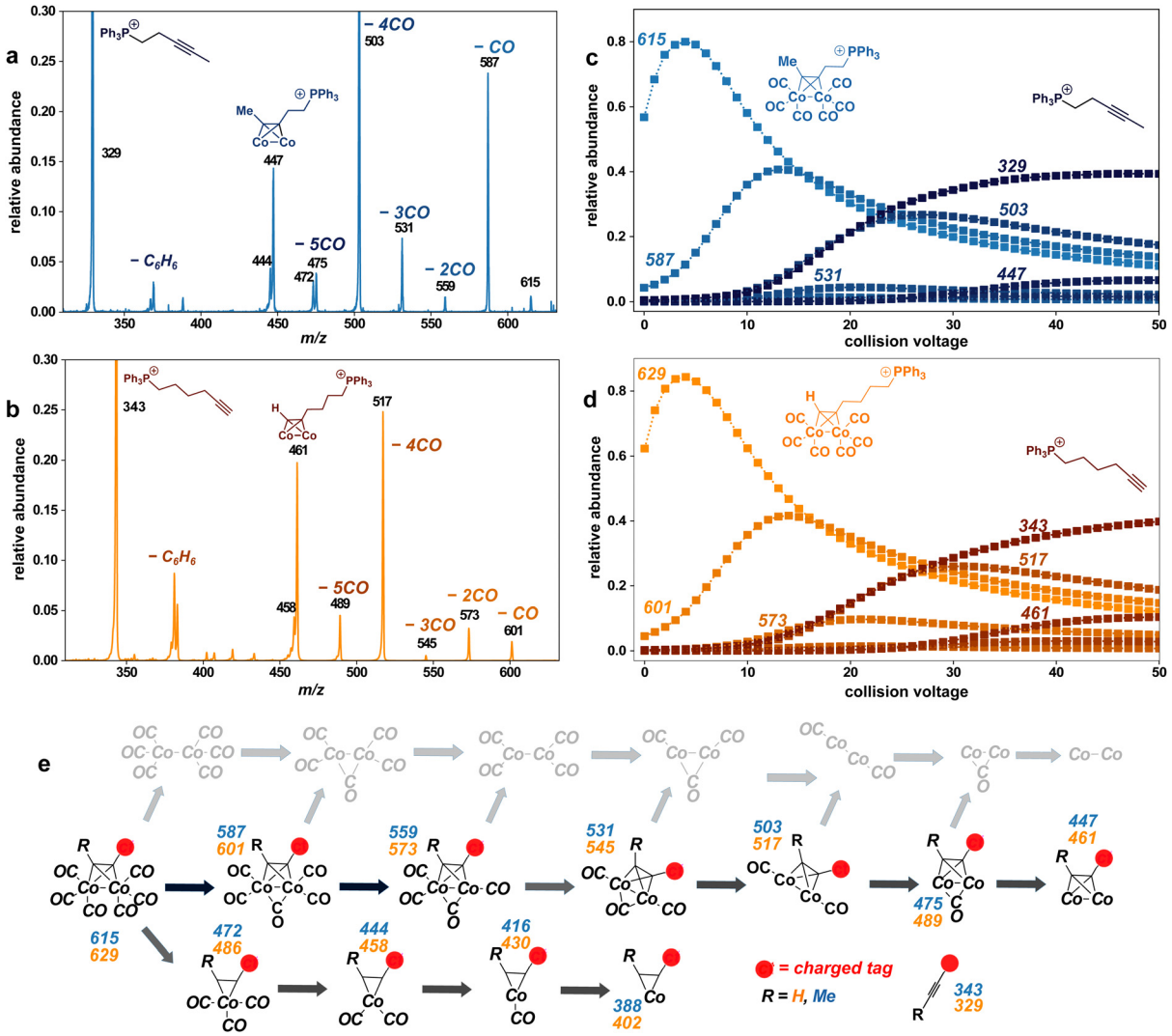

Fig. 4 CID experiments reveal the gas phase decomposition of **3** and **4**. Spectra (a) and (b) plot the *m/z* values of the daughter ions detected over the course of the experiment. Panels (c) and (d) plot the abundance of daughter ions as the collision voltage is increased. Predominant traces are labelled with the corresponding ion mass. Panel (e) shows the decomposition pathways and the *m/z* values for charged species that can be observed by MS labelled in blue (internal alkyne) and orange (terminal alkyne). The charged components of **3** and **4** are denoted by a red circle.

directly compare the pathways of the ionic fragmentation observed by MS to pathways involving neutral species (Fig. 5). Geometry optimizations were performed to obtain the minimum energy structure and electronic energy for each intermediate. The electronic dEs in Fig. 5 are very similar between the terminal and internal alkyne which agrees with the similarities observed between decomposition of **3** and **4**. The most probable first and second steps were found to be CO dissociation and the cleavage of the Co–Co bond is less energetically feasible than loss of CO. Computational results also suggest that as carbonyl ligands are lost, the terminal alkyne binds more tenaciously than the internal alkyne. The dE increases for removing the terminal alkynyl in later decomposition steps. This is also in agreement with CID data in Fig. 4 where the internal alkyne is removed slightly more easily than the terminal alkyne. Furthermore, the difference in stability between the complexes after loss of one *versus* two carbonyls is also reflected in the dE for steps 1 and 2 in the middle pathway of Fig. 5. The terminal alkyne proceeds through the first two CO losses with dEs of 133 and 107 kJ mol^{-1} for the first and second loss respectively, whereas the internal alkyne proceeds with a slightly lower energy of 130 kJ mol^{-1} for the first CO loss. The second loss of CO is significantly higher in the inernal alkyne, costing 120 kJ mol^{-1}. Hence, *m/z* 587 is a more prominent intermediate than *m/z* 601 (Fig. 4a and b). The calculated cost of removing an initial CO is similar to the known experimental BDE of CO from $Co_2(CO)_8$ measured to be 138 kJ mol^{-1}.[39]

2.4 Surface deposition simulations

Simulations involving the Si(111) surface identified additional advantages of an internal alkyne for deposition. The weakened alkyne–Co bond was found to strengthen the interaction between Co and the surface during precursor decomposition. Furthermore, the internal alkyne also shows reduced reactivity

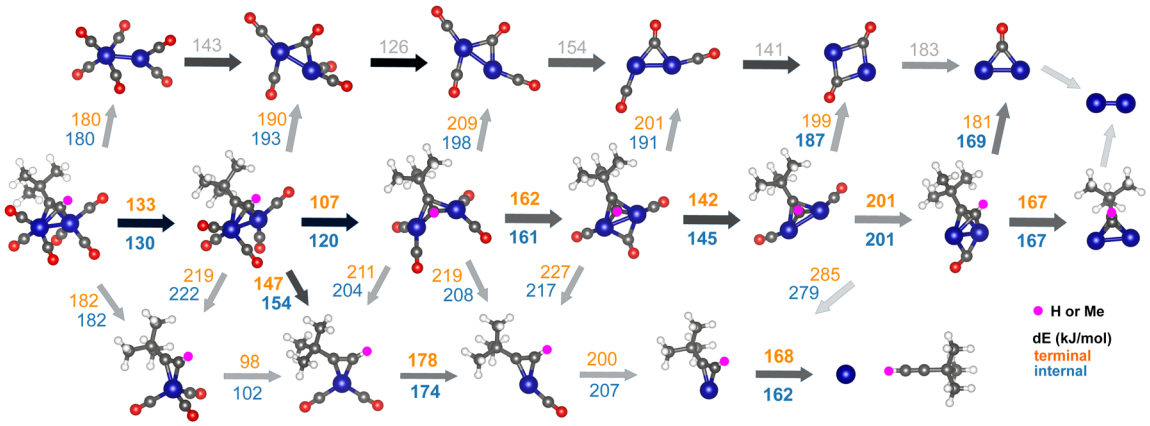

Fig. 5 The predominant decomposition pathways computed for CCTBA. Orange/top numbers represent dEs for terminal alkyne and blue/bottom numbers for the internal alkyne. A pink sphere represents the position of H or Me.

towards the silicone surface, suggesting a decrease in carbon-contamination during ALD.

Decomposition by sequential loss of carbonyls was simulated on Si(111) for CCTBA and CCTMA to identify the stabilizing role played by the surface (Fig. 6a). As in the gas phase, the carbonyl bond dissociation energies (BDE) are very similar between the internal and terminal alkyne. Strong chemisorption interactions formed in step 4 after the loss of three carbonyls (Fig. 6a).

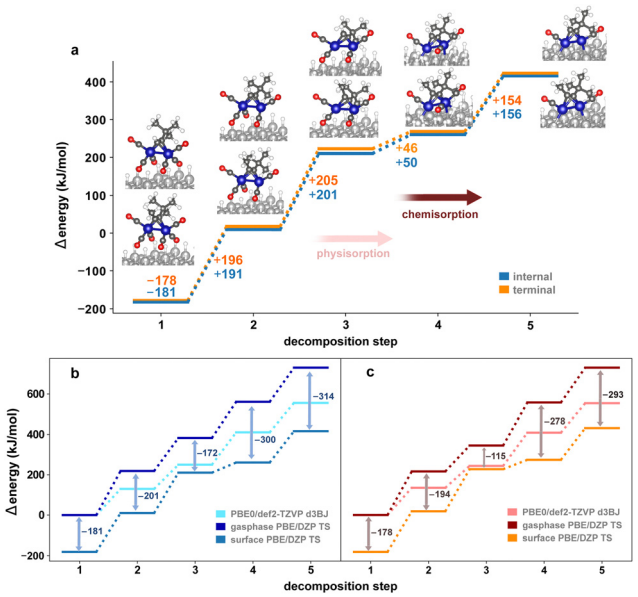

Fig. 6 Delta Es plotted for the initial deposition steps on an intact Si(111) surface. Panel (a) shows the decomposition steps of CCTMA (blue) and CCTBA (orange) on the surface with corresponding adsorption geometries for each step. The ddEs values are labeled in orange for CCTBA and blue for CCTMA. Red arrows mark the transition from physisorption to chemisorption as the Co sequentially loses CO. These energies were benchmarked against gas phase data for CCTMA (b) and CCTBA (c) and the energetic stabilization offered by the surface is marked by arrows and numbers at each step. Light blue (b) and salmon (c) denote phase data obtained with PBE0/def2-TZVP(d3BJ), dark blue (b) and dark red (c) mark gas phase data obtained with PBE/DZP(TS) which was also the method used for surface calculations (blue b, orange c).

Chemisorption may also take place in earlier decomposition steps in the presence of a surface defect or with an opportune collision. The dEs were heavily dependent on the functional used to assess the carbonyl BDEs. Calculating accurate BDEs of metal–carbonyl complexes requires adequate inclusion of electron correlation.[40] In the periodic calculations using PBE/DZP, the metal–carbonyl bond strength was overestimated in the gas phase compared to results from PBE0/def-TZVP calculations Fig. 6b and c. However, trends across reaction paths for both precursors were consistent between methods. Observing surface interactions at a molecular level is a useful tool in understanding the deposition of these ALD precursors.

Over the course of precursor decomposition, the surface played an increasing role in stabilizing the precursor (Fig. 6b). For both precursors, step 3 of deposition shows a weakened surface interaction relative to the other steps (Fig. 6b and c, −172 and −115 kJ mol^{-1}) which precedes step 4 where chemisorption interactions start to form and surface interactions strengthen significantly. Fig. 6b and c show that or every decomposition step, CCTMA shows stronger interactions with the surface than CCTBA. These trends suggest that the internal alkyne in CCTMA

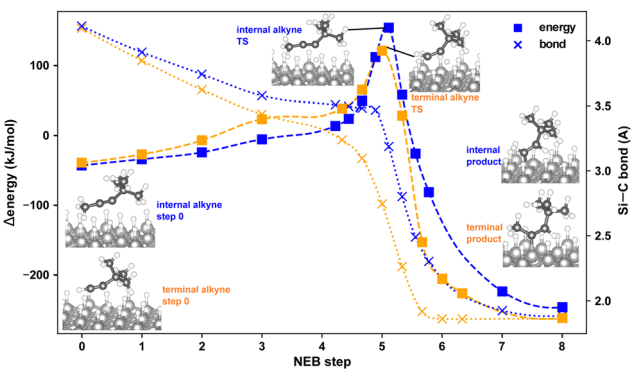

Fig. 7 NEB results for hydrosilation of each alkyne on Si(111) surface. The bond length (x's) of the newly forming Si–C bond and delta Es (squares) for the internal alkyne (blue) and the terminal alkyne (orange) are plotted over the course of the reaction. Snapshots for the initial, transition state and the final step of the NEB calculation are labelled on the plot.

allows Co to interact more strongly with the surface while a terminal alkyne is more tenaciously bound to the metal centers as observed in the experimental results from CID.

Finally, the reactivity of the terminal and internal alkyne ligand with Si(111) was investigated. NEB calculations were performed for an uncatalyzed hydrosilation reaction step on Si(111) (Fig. 7). As expected, the reaction barrier for the terminal alkyne (120 kJ mol^{-1}) is lower than the internal alkyne (154 kJ mol^{-1}), supporting decreased reactivity between the surface and an internal alkyne. The newly forming carbon–silicon bond lengths are plotted over the course of the reaction path, showing a shorter bond distance for the terminal alkynyl carbon than the internal alkyne (yellow dotted lines in Fig. 7 *versus* blue dotted lines). The internal alkyne remains farther from the surface until the transition state is complete, likely due to the steric hindrance introduced by the methyl group. These findings support an expected decrease in carbon impurities embedded into the Si surface in the presence of an internal alkynyl ligand.

3 Conclusions

The charged analogs of CCTBA and CCTMA precursors displayed trends that were consistent with computational results for the neutral species. Furthermore, the terminal and internal alkynyl cobalt carbonyl complexes shared very similar decomposition pathways both in the gas phase and on the surface. However, the experimental and computational data indicate that the internal alkyne is lost from the complex at a lower energy than the terminal alkyne while also boasting a reduced reactivity with the Si(111) surface. Easy removal of the alkynyl ligand may be more desirable for ALD requiring low substrate temperatures while also reducing the amount of carbon embedded in the film. In computational studies, CCTMA showed stronger interactions with Si(111) during carbonyl loss compared to CCTBA. Finally, the reaction barrier of inserting each alkyne into a Si–H bond on the surface shows a higher barrier for a methylated alkyne, suggesting a lower rate of reaction with the surface and thus likely decreased carbon impurities embedded in Si during ALD.

This work suggests that internal alkyne alternatives will make deposition at lower temperatures more efficient due to easier removal of the alkynyl ligand and more targeted reactivity with the surface. Future work should involve the monitoring of other alkynes and perhaps new metal carbonyls to fully explore the potential of alkynyl ligands for ALD. CID data gave a first glimpse at what product ion species form in the gas phase under energetic stress and is a valuable tool for accessing gas phase information about precursor reactivity. ALD of CCTMA on Si should be performed and benchmarked against CCTBA to test the effects of temperature and measure the carbon-content of the deposited films. Internal alkynes are as affordable as the terminal TBA (*e.g.* 2-butyne, 2-pentyne, 2- and 3-hexyne are all cheaper than the $30 per g cost of TBA) (Table S1, ESI†). Testing the behavior of these simple alkynes will determine whether an inexpensive alternative to TBA can be paired with cobalt carbonyl for ALD to optimize the deposition of Co.

Author contributions

Sofia Donnecke: conceptualization, investigation, formal analysis, visualization, writing – original draft; Mathias Paul: investigation, analysis, editing; Peter Williams: investigation; Serena Chan: investigation, data curation; Veronica Tse: investigation, data curation; Jigyasa Sachdeva: investigation; Allen G. Oliver: investigation; Irina Paci: conceptualization, funding acquisition, resources, supervision, writing – review and editing; J. Scott McIndoe: conceptualization, resources, supervision, writing – review and editing.

Conflicts of interest

There are no conflicts to declare.

Acknowledgements

We acknowledge the support of the Natural Sciences and Engineering Research Council of Canada (NSERC) and SEASTAR CHEMICALS Inc. This research was enabled in part by support provided by WestGrid (**https://www.westgrid.ca**) and Compute Canada (**https://www.computecanada.ca**).

References

1 J. Lu, H.-C. Ha, P. Ma, S. Ganguli, J. F. Aubuchon, S.-H. Yu and M. K. Narasimhan, *Cobalt deposition on barrier surfaces*, 2015, **https://patents.google.com/patent/US9051641B2**.

2 T. J. Knisley, L. C. Kalutarage and C. H. Winter, *Precursors and chemistry for the atomic layer deposition of metallic first row transition metal films*, 2013, **https://digitalcommons.wayne.edu/oa_dissertations**.

3 X. Luo, C.-Y. Chen, T.-F. M. Chang, K. Lee, T. Park, J. Lee, J. Kim, J. Kim, N. Kwak, S. Yeom and H. Jeon, *Jpn. J. Appl. Phys.*, 2008, **47**, 5396.

4 C. A. Cooper, S. Ivanov and M.-S. Kim, Disubstituted Alkyne Dicobalt Hexacarbonyl Compounds, Method of Making and Method of Use Thereof, 2018, **https://patents.google.com/patent/US20180134738A1/en**.

5 B. Han, K. H. Choi, K. Park, W. S. Han and W. J. Lee, *Electrochem. Solid-State Lett.*, 2012, **15**, D14.

6 S. B. Kang, H. S. Kim, K. J. Moon, W. H. Sohn, G. H. Choi, S. H. Kim, N. J. Bae, U. I. Chung and J. T. Moon, *Tech. Dig. - Int. Electron Devices Meet.*, 2003, 501–504.

7 J. H. Park, D. Y. Moon, D. S. Han, Y. J. Kang, S. R. Shin, H. T. Jeon and J. W. Park, *Surf. Coat. Technol.*, 2014, **259**, 98–101.

8 A. E. Kaloyeros, Y. Pan, J. Goff and B. Arkles, *ECS J. Solid State Sci. Technol.*, 2019, **8**, P119–P152.

9 H. W. Sternberg, J. G. Shukys, C. D. Donne, R. Markby, R. A. Friedel and I. Wender, *J. Am. Chem. Soc.*, 1959, **81**, 2339–2342.
10 J. Kwon, M. Saly, R. K. Kanjolia and Y. J. Chabal, *Chem. Mater.*, 2011, **23**, 2068–2074.
11 M. J. Went, *Advances in Organometallic Chemistry*, Academic Press, 1997, vol. **41**, pp. 69–125.
12 R. W. Johnson, A. Hultqvist and S. F. Bent, *Mater. Today*, 2014, **17**, 236–246.
13 S. T. Barry, A. V. Teplyakov and F. Zaera, *Acc. Chem. Res.*, 2018, **51**, 800–809.
14 D. N. Goldstein, J. A. McCormick and S. M. George, *J. Phys. Chem. C*, 2008, **112**, 19530–19539.
15 R. Matero, A. Rahtu and M. Ritala, *Langmuir*, 2005, **21**, 3498–3502.
16 J. Niinistö, A. Rahtu, M. Putkonen, M. Ritala, M. Leskelä and L. Niinistö, *Langmuir*, 2005, **21**, 7321–7325.
17 R. Freitas, G. Gueorguiev, F. de Brito Mota, C. de Castilho, S. Stafström and A. Kakanakova-Georgieva, *Chem. Phys. Lett.*, 2013, **583**, 119–124.
18 D. G. Sangiovanni, R. Faccio, G. K. Gueorguiev and A. Kakanakova-Georgieva, *Phys. Chem. Chem. Phys.*, 2023, **25**, 829–837.
19 K. Bernal Ramos, M. J. Saly and Y. J. Chabal, *Coord. Chem. Rev.*, 2013, **257**, 3271–3281.
20 D. M. Chisholm and J. Scott McIndoe, *Dalton Trans.*, 2008, 3933–3945.
21 M. A. Henderson, J. Luo, A. Oliver and J. S. Mcindoe, *Organometallics*, 2011, **30**, 5471–5479.
22 A. Joshi, C. Killeen, T. Thiessen, H. Zijlstra and S. McIndoe, *J. Mass Spectrom.*, 2022, **57**, e4740.
23 S. Grimme, J. Antony, S. Ehrlich and H. Krieg, *J. Chem. Phys.*, 2010, **132**, 154104.
24 M. Valiev, E. J. Bylaska, N. Govind, K. Kowalski, T. P. Straatsma, H. J. Van Dam, D. Wang, J. Nieplocha, E. Apra, T. L. Windus and W. A. De Jong, *Comput. Phys. Commun.*, 2010, **181**, 1477–1489.
25 J. M. Soler, E. Artacho, J. D. Gale, A. García, J. Junquera, P. Ordejón and D. Sánchez-Portal, *J. Phys.: Condens. Matter*, 2002, **14**, 2745–2779.
26 N. Troullier and J. L. Martins, *Phys. Rev. B: Condens. Matter Mater. Phys.*, 1991, **43**, 8861–8869.
27 D. J. Evans and B. L. Holian, *J. Chem. Phys.*, 1985, **83**, 4069–4074.
28 A. Hjorth Larsen, J. JØrgen Mortensen, J. Blomqvist, I. E. Castelli, R. Christensen, M. Dupoll, J. Friis, M. N. Groves, B. Hammer, C. Hargus, E. D. Hermes, P. C. Jennings, P. Bjerre Jensen, J. Kermode, J. R. Kitchin, E. Leonhard Kolsbjerg, J. Kubal, K. Kaasbjerg, S. Lysgaard, J. Bergmann Maronsson, T. Maxson, T. Olsen, L. Pastewka, A. Peterson, C. Rostgaard, J. SchiØtz, O. Schütt, M. Strange, K. S. Thygesen, T. Vegge, L. Vilhelmsen, M. Walter, Z. Zeng and K. W. Jacobsen, The atomic simulation environment-A Python library for working with atoms, 2017, **https://iopscience.iop.org/article/10.1088/1361-648X/aa680ehttps://iopscience.iop.org/article/10.1088/1361-648X/aa680e/meta**.
29 G. T. Thomas, S. Donnecke, I. C. Chagunda and J. S. McIndoe, *Chem.: Methods*, 2022, **2**, e202100101.
30 K. L. Vikse, Z. Ahmadi, J. Luo, N. Van Der Waals, K. Daze, N. Taylor and J. S. McIndoe, *Int. J. Mass Spectrom.*, 2012, **323–324**, 8–13.
31 J. Burés, *Angew. Chem., Int. Ed.*, 2016, **55**, 16084–16087.
32 P. C. Leung and P. Coppens, *Acta Crystallogr., Sect. B: Struct. Sci.*, 1983, **39**, 535–542.
33 R. L. Sweany and T. L. Brown, *Inorg. Chem.*, 1977, **16**, 415–421.
34 T. Y. Garcia, J. C. Fettinger, M. M. Olmstead and A. L. Balch, *Chem. Commun.*, 2009, 7143–7145.
35 M. I. Bruce, M. Gaudio, B. C. Hall, B. K. Nicholson, G. J. Perkins, B. W. Skelton and A. H. White, *Z. Anorg. Allg. Chem.*, 2011, **637**, 1207–1212.
36 K. Nicholas and R. Pettit, *Tetrahedron Lett.*, 1971, **12**, 3475–3478.
37 R. H. Crabtree, *Appl. Organomet. Chem.*, 2010, **24**, 667.
38 M. Kinebuchi, R. Uematsu and K. Tanino, *Tetrahedron Lett.*, 2017, **58**, 1382–1386.
39 A. Cartner, B. Robinson and P. J. Gardner, *J. Chem. Soc., Chem. Commun.*, 1973.
40 J. Li, G. Schreckenbach and T. Ziegler, *J. Am. Chem. Soc.*, 1995, **117**, 486–494.